

# Changing Climate Impacts: Analytics to Characterize Extreme Temperature Events in California

Nabig Chaudhry

May 6, 2022

## **Abstract**

Climate change will alter extreme weather event exposure and consequently intensify climate impact on human and natural systems. Assessment of exposure and impact is critical for understanding system vulnerabilities and building adaptation and resilience to climate change. However, this information is complex, difficult to use, and often too broad for stakeholders – many of whom require very context-specific information on particular geographies, events types, or critical thresholds. One promising solution is to develop customizable analytics that demonstrate scientifically defensible approaches for extracting context-specific information for decision applications, which can be adapted to different geographies and user-specific metrics. In this paper, I demonstrate the application of customizable analytics to quantify extreme weather event exposure by evaluating the return value of 1-in-10-year extreme temperature events in California from periods starting in 1980 and ending in 2100. Through extreme value analysis supported by L-moments and the generalized extreme value distribution, I produce data products that detail return values of 1-in-10-year extreme temperature events across two global climate models (CESM2 and CNRM-ESM2-1), one projected scenario (SSP3-7.0), five 20-year temporal periods (1980-1999, 2020-2039, 2040-2059, 2060-2079, and 2080-2099), and every 9-km gridded area in California. The data products I produced highlight an approach to using customizable analytics to deliver decision-relevant insights on climate impact to stakeholders.

# 1 Introduction

Climate change has already and will continue to result in a change in the frequency and magnitude of extreme weather events [1]. Understanding extreme weather events and any changes in their occurrence is critical because of the disproportionate impact these events have on human and natural systems and the relevance they carry for risk assessments, design standards, resource planning, and public policy [1, 2]. By connecting extreme weather event exposure to system sensitivities, climate impact from extreme weather events can be distilled and propel efforts on system resilience, adaptive capacity, and vulnerability assessments. [3].

Quantifying the exposure to extreme weather events is the first step to understanding vulnerabilities and how climate change may be altering climate impact and risk [3]. One approach to quantifying this exposure is through frequency analysis, which aims to estimate how often a certain value of interest or event will occur, usually in correspondence to a return period or return value [4, 5]. By using extreme value analysis (EVA) to conduct frequency analysis on historical observations, the likelihood and magnitude of extreme weather events can be estimated both historically and probabilistically into the future [6, 4]. The exposure to extreme weather events and the risk they carry, however, is rapidly changing due to climate change, which has made climate observational data non-stationary and rendered EVA and frequency analysis based only on historical data unreliable for understanding future risk [7, 8]. Thus, to fully understand the frequency and magnitude of extreme weather events and produce information that can be used for tasks such as design standards or risk assessments, the context in which these events are changing across spatial and temporal scales due to climate change is essential [8, 9, 2].

Stakeholders, especially those managing human systems such as energy and water, need tools to quantify the exposure (and change in exposure) to extreme weather events alongside system sensitivities in order to evaluate climate impact [8, 9]. However, these stakeholders often run into a “practitioner’s dilemma” where even though climate data is widely available, there is confusion on how to pick appropriate data, assess it properly, and utilize it for context-specific applications relating to particular geographies, event types, thresholds, and more [10]. To address the need for context-specific and decision-relevant insights that stakeholders are looking for, these tools need to be easy-to-use and customizable for a myriad of context-specific applications [10]. Likewise,

given the lack of stationarity in climate data, these customizable tools need to provide stakeholders with flexibility to choose and extend across different time periods in order to both improve systems that exist today and also to build systems that account for extreme events into the future [7, 11].

In this paper, in partnership with the Cal-Adapt Analytics Engine project (*analytics.cal-adapt.org*), a climate data platform being developed to support energy sector needs for actionable data, I propose a foundational set of customizable analytics to characterize extreme events and address the need of stakeholders for decision-relevant insights regarding extreme weather events [10]. The goal of this paper is to showcase a proof of concept in terms of how a scientifically-defensible and customizable set of analytics can be applied to pull decision-relevant and context-specific insights. The paper establishes a flexible and scientifically-defensible methodological approach for EVA using L-moments and generalized extreme value distributions on historical and projected climate models. This is an approach that has been validated and carried out in many other studies conducting frequency analysis of extreme weather events and can be adapted to a variety of specific context-specific metrics [2, 12, 13, 14, 15, 4]. The customizable analytics based on this methodological approach are built using statistical and computational tools and ultimately take downscaled climate models and EVA and produce frequency analysis on extreme weather events spatially across California and over historical and projected temporal periods.

This paper begins by outlining the analytics for quantifying exposure to extreme weather events along with the data products produced. Following this foundation, to demonstrate application I apply this approach to a particular energy sector use-case:

**Return Value of Extreme Temperature Event.** I calculate the return values for a 1-hour extreme temperature event with a 10-year return periods (i.e., 1-in-10-year events) across California for different temporal periods while highlighting the changes in extreme weather event exposure and climate impact over time.

Extreme temperatures are highly relevant for energy stakeholders as they can not only increase electricity demand but also directly cause issues such as system disruptions, system reliability issues, and capacity loss [3]. For electricity generation systems ranging from thermoelectric to solar, high ambient air temperature can reduce efficiency, generation capacity, and potential capacity [3]. For transmission and distribution systems such as transformers and power

lines, high temperatures can accelerate aging, decrease capacity, and reduce transmission efficiency [3]. The use of 10-year return periods in this use-case is also exercised specifically with energy sector stakeholders in mind, as a 1-in-10-year event is a common probability for the incorporation of extreme weather events in load profiles and system planning by energy entities such as Western Electricity Coordinating Council [11, 16]. Thus, the paper employs this particular energy sector use-case as means of underscoring the array of decision-relevant insights that this set of customizable analytics can provide.

All analytics used for this project in terms of code, analysis, data products, figures, and more is available open-source for interested parties and relevant stakeholders to replicate, reproduce, and modify to their specific use-cases in the following Github repository: [github.com/nabigac/masters\\_project](https://github.com/nabigac/masters_project) [17].

## 2 Data

The data in this study comes from dynamically downscaled global climate models from the 6th phase of the Coupled Model Intercomparison Project (CMIP6). The climate models were dynamically downscaled to a higher resolution signal using Weather Research and Forecasting (WRF) model simulations across the western United States [18]. Though climate models can carry a large degree of uncertainty they do offer plausible future scenarios that can be useful for understanding changes to climate exposure and impact [8]. I used dynamically downscaled historical and future projected data from the following CMIP6 Global Climate Models (GCMs) and corresponding Shared Socioeconomic Pathways (SSPs):

CMIP6 GCMs	
GCM Name	Data Used
CESM2	Historical and SSP3-7.0
CNRM-ESM2-1	Historical and SSP3-7.0

The data includes both historical and future projected hourly temperature data with future projected data encompassing the SSP3-7.0 scenario, a medium-to-high end forcing future where there is no mitigation beyond what has occurred [19]. The data has a 9 kilometer (km) spatial resolution across western United States but is subset spatially to California. It is temporally subset into five 20-year temporal periods (inclusive): 1980-1999 (historical

data), 2020-2039 (projected data), 2040-2059 (projected data), 2060-2079 (projected data), and 2080-2099 (projected data). The 1980-1999 temporal period represents the baseline from which extreme weather event exposure and climate impact changes are assessed. I used 20-year temporal periods to ensure an adequate and consistent sample size for the 1-in-10-year return value calculations and to accommodate any non-stationary trends that may exist in the climate data [7].

### 3 Methods

To characterize extremes, conduct frequency analysis, and pull decision-relevant insights, I use extreme value analysis (EVA). First, I utilize a standard EVA block-maxima approach with block size set to 1 calendar year and pull the annual maximum series (AMS) from each grid cell of hourly temperature data [2]. Second, for each of those samples of annual extremes, I fit a generalized extreme value (GEV) distribution using the L-moments method [20, 2, 4].

L-moments, which are linear combinations of order statistics, are a sequence of statistics used to summarize the shape of a probability distribution [20, 12, 15]. Similar to conventional moments like the mean or variance, sample L-moments summarize properties such as location, scale, skewness, and kurtosis and can be employed to estimate parameters of a distribution [20, 12]. L-moments are preferred because, in comparison to conventional moments, they are more robust with outliers when estimated from a sample, and in comparison to maximum likelihood estimates are more computationally straightforward and often more accurate in parameter estimates for small sample sizes [20, 12, 2].

I use the GEV distribution for its theoretical basis given that for a sample of independent and identically distributed variables, the distribution of maximums of that sample converge to the GEV distribution, as the sample size approaches infinity [2]. The distribution has three adjustable parameters:  $\xi$  (*location*),  $\alpha$  (*shape*), and  $k$  (*scale*) [2].

Lastly, in accordance with EVA, I utilize the cumulative distribution function, and subsequently the percent point function, otherwise known as the inverse cumulative distribution function, from the GEV to calculate the return values [2]. For a cumulative distribution function  $F(x)$ , the return value for a given time  $T$  (usually in years) is the value of  $X$  that is exceeded once every  $T$  units [2]. The return value  $X$  for a given  $T$  unit is thus the

value of  $x$  that meets  $F(x) = 1 - 1/T$  [2]. On the other hand, the return period is equal to the average amount of waiting time between extremes of size  $x$  or larger [2]. Hence, the return period for a given value of  $x$  and time  $T$  is  $T = 1/[1 - F(x)]$  [2].

To understand the goodness-of-fit of the GEV distribution to the AMS and provide strength of evidence for return values and return periods calculated, I apply the Kolmogorov–Smirnov (KS) test for every AMS at each respective grid cell [13]. One thing to note is that though I use the GEV distribution in this paper there may be other extreme value distributions, depending on the particular grid cell, that also pass the goodness-of-fit test or are a better model than the GEV [14]. Model selection techniques such as the corrected Akaike information criterion (AICc) could be used in conjunction with goodness-of-fit tests like the KS test to ensure the best model is fitted to the AMS at every respective grid cell [5, 7].

The analytics built and applied in this study were coded entirely using Python and relevant core packages such as xarray and numpy. L-moments are formulated from the AMS at each grid cell through the lmoments3 package, which is the Python implementation of the lmoments.f library originally created by J. R. M. Hosking [21]. L-moments, and associated parameters, are fitted to a GEV distribution using the scipy.stats package from which return values are calculated. The corresponding visualizations are created using geospatial processing packages such as cartopy and hvplot. All code is reproducible, customizable, and available open-source in the Github repository [17].

## 4 Results and Discussion

For each GCM (CESM2 and CNRM-ESM2-1), 9-km grid cell, and 20-year temporal period (1980-1999, 2020-2039, 2040-2059, 2060-2079, and 2080-2099), I calculated return values for a 1-in-10-year event. These return values represent the magnitude of 1-in-10-year extreme temperature events that occur for 1-hour, as the AMS was pulled from hourly temperature data. These particular return values can be used by energy stakeholders like system planners and grid operators for building 10-year demand and load profiles, assessing grid system stability issues, quantifying efficiency and capacity losses from extreme weather events, and more [3, 16, 11].

Final data products from the analytics are datasets and visualizations

shown as either gridded geospatial maps such as in Figures 1 or 4 or aggregate plots such as Figure 5. All data used to produce visualizations, along with additional parameters such as confidence intervals for each return value, can be found as netCDF datasets in the Github repository under the *data/final\_for\_analysis* folder [17]. All gridded geospatial maps are available as interactive HTML applications, which allow one to view the specific result of any particular 9-km grid cell or latitude and longitude coordinates, and can be found in the Github repository under the *images/interactive* folder [17].

Figures 1 and 2 show gridded geospatial results of the p-value from the KS test. The null hypothesis, in this case, is that the two distributions are identical – those two distributions being the AMS and the fitted GEV distribution at each grid cell. With a significance level of 0.05, any value above 0.05 presents evidence that the two distributions are identical and would mean failure to reject the null hypothesis. In the following table, based on the minimum p-value obtained across all grid cells, both climate models presented higher p-values than 0.05 for all temporal periods:

Minimum KS Test P-Value Across All Grid Cells		
Time Period	CESM2	CNRM-ESM2-1
Historical 1980-99	0.055665	0.059451
SSP3-7.0 2020-39	0.263161	0.257351
SSP3-7.0 2040-59	0.307685	0.161346
SSP3-7.0 2060-79	0.173826	0.289586
SSP3-7.0 2080-99	0.260631	0.193136

This presents evidence that the two distributions are identical and the GEV distribution is a good fit for the data across both GCMs, all locations, and all temporal periods. This trend is further detailed in the gridded geospatial plots, where in Figures 1 and 2, the gridded area for all the temporal periods is overwhelmingly dark blue meaning that for most grid cells there is strong evidence that the GEV distribution is a good fit for the data. The historical 1980-1999 temporal period had the lowest minimum p-values across all temporal periods for both models, which could signal that there are particular grid cells for that temporal period where another probability distribution may provide an even better fit for the AMS. For instance, Figure 2 for the CNRM-ESM2-1 GCM presents an idea of where these cells are located by showing p-values that are closer to 0.05 around eastern California.

Overall, however, both the table and corresponding figures present evidence that the GEV distribution is a good fit for the data.

Figures 3 and 4 show gridded geospatial results of the return values for a 1-in-10-year event. Both Figures 3 and 4 for all temporal periods showcase generally higher return values (i.e., higher temperatures) for southern California compared to northern California and for the Central Valley region compared to the Sierra Nevada mountain range. Both figures visually also demonstrate a gradual trend of darker red (i.e., higher return values) as the temporal periods get closer to 2100.

Figure 5 shows aggregate return value data in a box plot excluding any latitude and longitude information by GCM and temporal period. In both Figures 5(a) and 5(b), there is a general trend showing the median, max, and min of the aggregate return values getting higher from the initial 20-year temporal period (1980-1999) to the final (2080-2099). For the CESM2 GCM in Figure 5(a) there does appear to be less distinctive changes between the 2020-2039, 2040-2059, and 2060-2079 temporal periods – a trend also observed in Figure 6(a). This trend difference along with median, max, and min value differences between the two GCMs in Figures 5(a) and 5(b) highlights some of the variability and uncertainty that exists in return value calculations between different GCMs.

Figure 6 shows aggregate return value data ordered from least to greatest on a line plot excluding any latitude and longitude information by GCM and temporal period. In both Figures 6(a) and 6(b), there is a general trend of increasing aggregate ordered return values from the initial 20-year temporal period (1980-1999) to the final (2080-2099). For the CESM2 GCM in Figure 6(a) the difference is most stark between the 1980-1999 temporal period and the 2080-2099 temporal period, whereas the temporal periods in between appear to be less distinct from one another. For the CNRM-ESM2-1 GCM in Figure 6(b) there appears to be a more uniform spread as the temporal periods go from 1980-1999 to 2080-2099. Overall, these line plots showcase how the full range of return values is generally increasing from the baseline 1980-1999 temporal period.

Figures 7 and 8 show gridded geospatial results of the percent change between the baseline temporal period (1980-1999) and one of the future projected temporal periods. Similarly to Figures 3 and 4, there is a general trend for both GCMs where the map is a darker shade of red (i.e., greater percent change) for Figures 7(d) and 8(d) comparing 1980-1999 to 2080-2099 versus Figures 7(a) and 8(a) comparing 1980-1999 to 2020-2039. The

magnitude of percent change for both GCMs appears greater in parts of northern and western California, especially along the Sierra Nevada mountain range.

In relation to the original application use-case relevant to energy sector stakeholders, these results and data products demonstrate how this set of customizable analytics can be applied to pull specific decision-relevant insights corresponding to 10-year return periods and extreme temperature events. For instance, take an example where an energy sector stakeholder like a utility system planner is assessing how much grid capacity will be lost in northern California by 2050 given capacity losses in power lines caused by extreme weather events. Based on findings by the California Energy Commission (CEC), an exceedance of ambient air temperature of  $37.78^{\circ}\text{C}$  produces a 7-8% capacity loss for power lines below their normal design rating [3]. Using this information, the system planner can map out where power lines with those design ratings are located in California according to latitude and longitude coordinates. Employing the data products (in the form of return value datasets or interactive geospatial maps) and modifying the analytics to fit this specific context, the stakeholder can discern which grid cell locations with said power lines will see a return value greater than  $37.78^{\circ}\text{C}$  for a 1-in-10-year event for the 2040-2059 temporal period for one or both of the GCMs. The initial approach and results that customize the analytics in this paper for this context-specific example is demonstrated for both GCMs in Figure 9.

This opportunity for localized and decision-relevant insights provides a fundamental step in understanding climate impact. By assessing the exposure that particular locations will have to extreme temperature events and how those relate to the sensitivity of power lines and other energy sector use-cases, the stakeholder can produce valuable conclusions on the climate impact on the energy system [3, 11]. Furthermore distilling where precisely the impact is taking place along with the associated vulnerabilities also grants insights on how and where adaptation and resilience measures could be deployed. With the example on power lines, once the stakeholders knows which power lines with normal design ratings will be exposed to temperature events greater than  $37.78^{\circ}\text{C}$  they can then reinforce or upgrade those particular power lines and build adaptive capacity against capacity losses from extreme temperature events [3].

The analytics performed in this paper and for this energy sector use-case can also be customized and expanded to assess non-energy sector contexts, different return values and return periods, specific locations, and varieties

of temporal periods. Thus, further underscoring how these customizable analytics can go beyond the initial foundational approach laid out in this paper and be employed for building context-specific and decision-relevant tools for stakeholders.

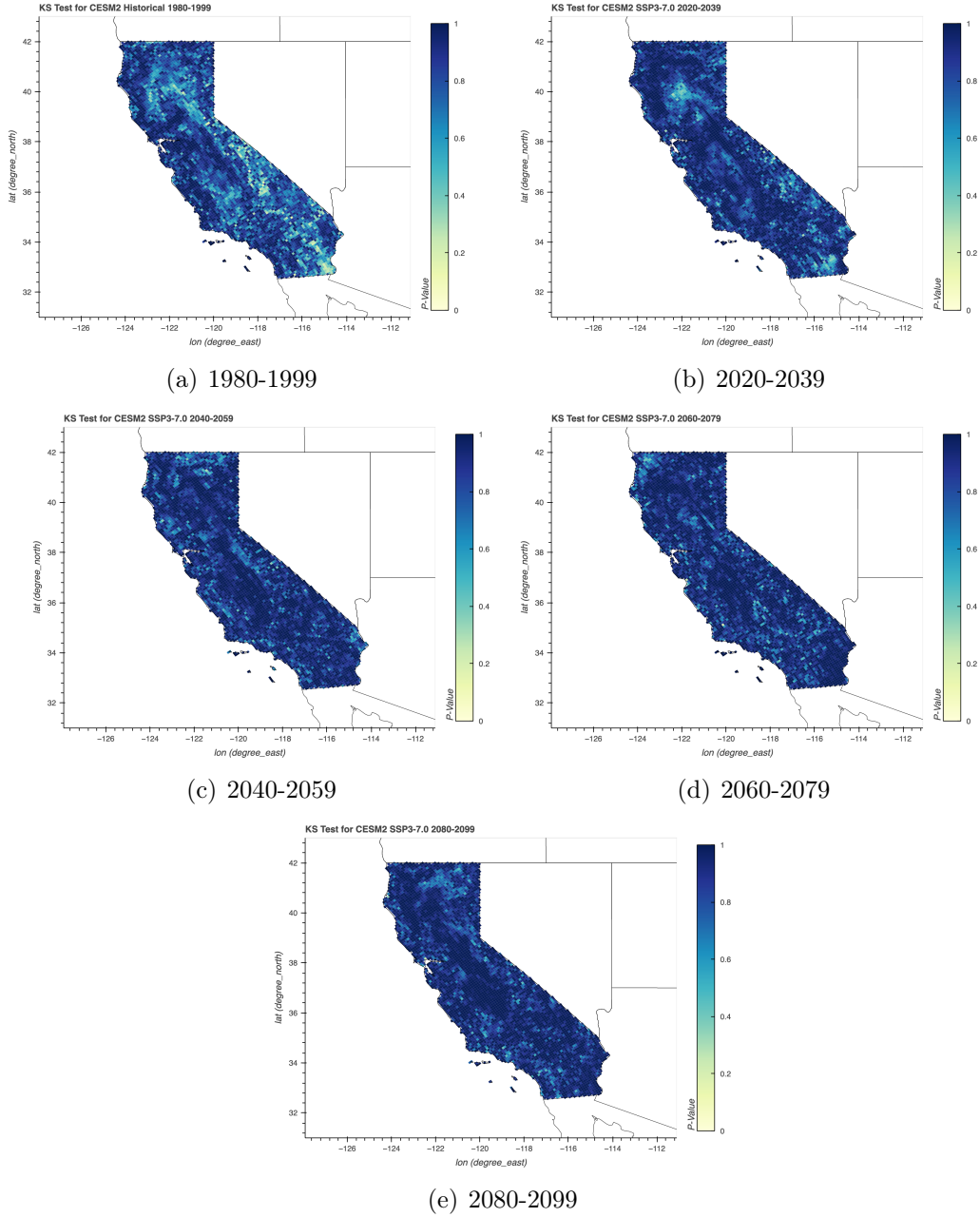


Figure 1: **CESM2 KS Test.** Geospatial map of p-value results from KS test for each 20-year temporal period. Interactive versions can be found in Github repository under the *images/interactive/ks\_test* folder [17].

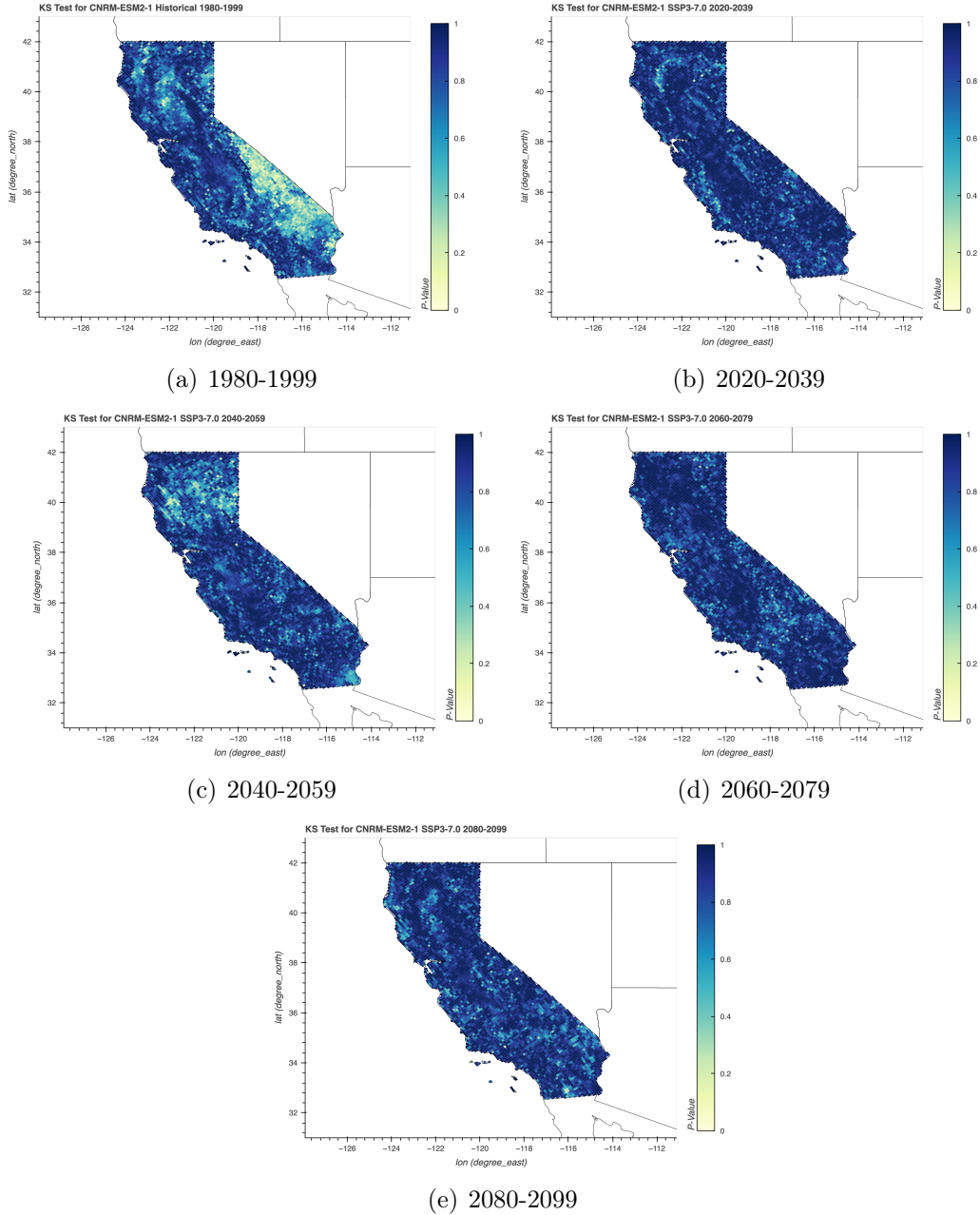
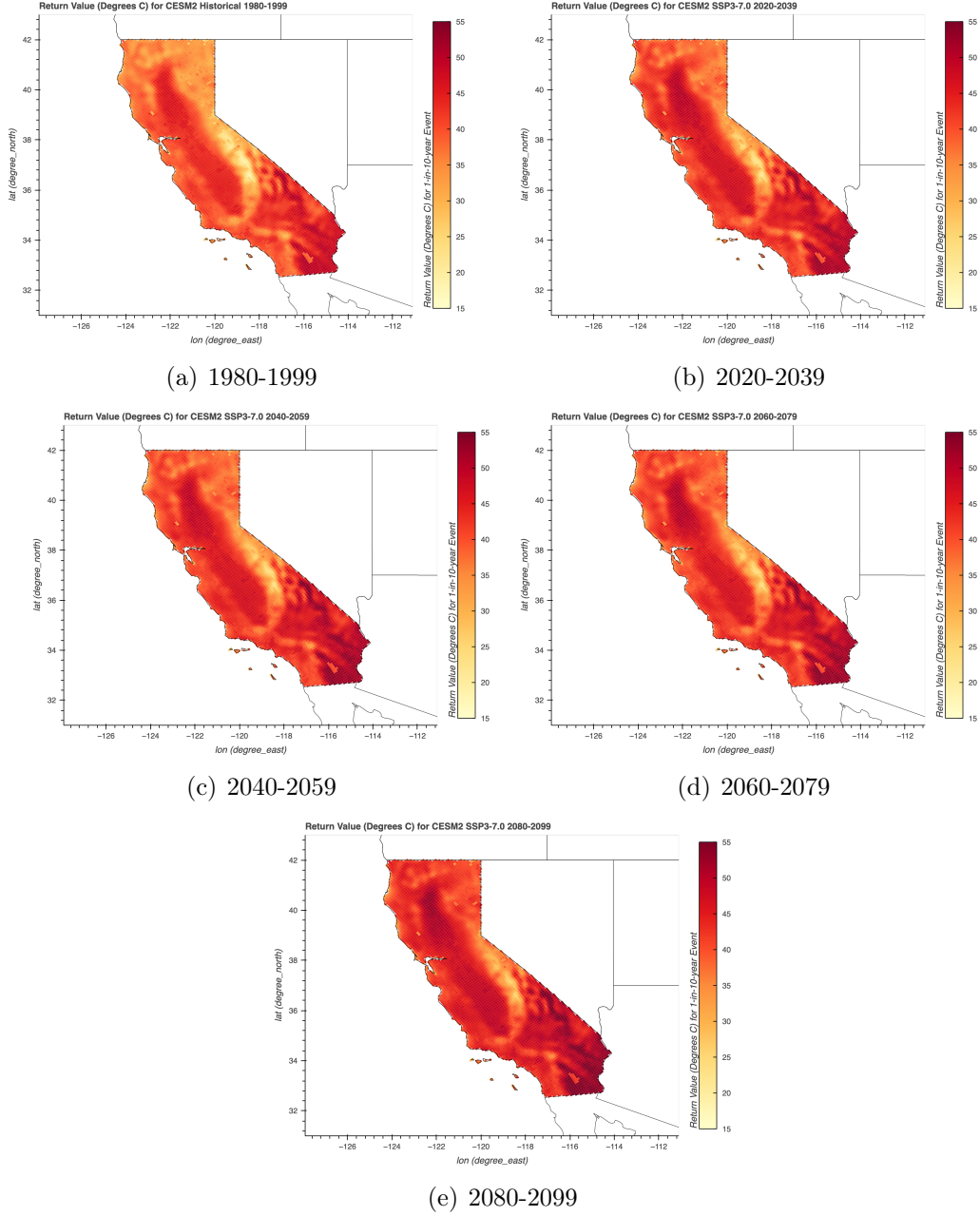
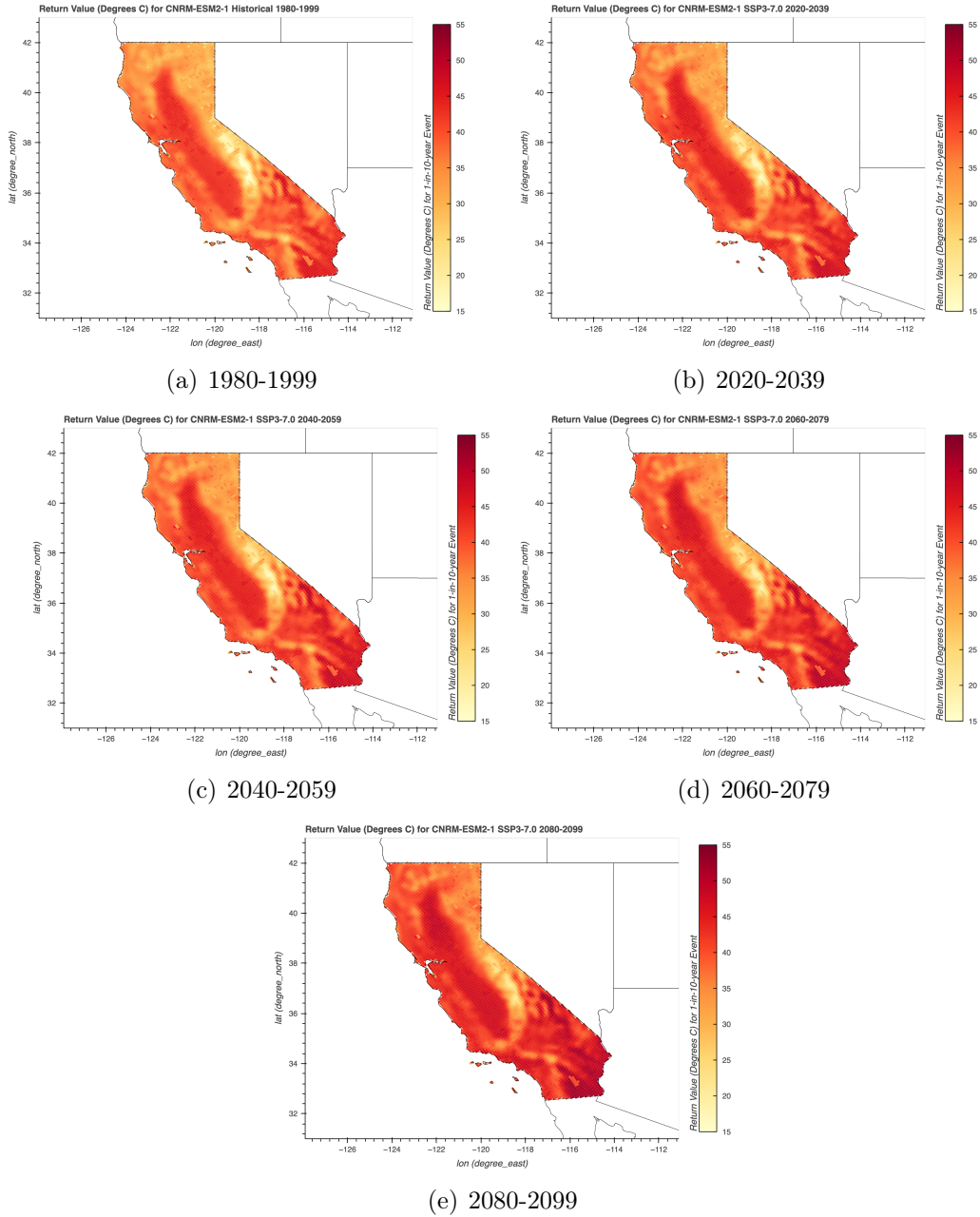


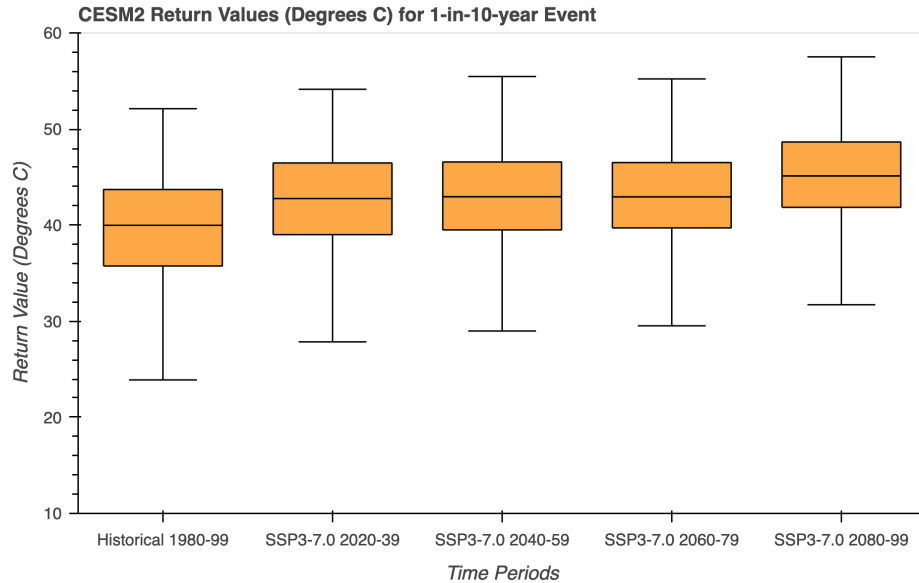
Figure 2: **CNRM-ESM2-1 KS Test.** Geospatial map of p-value results from KS test for each 20-year temporal period. Interactive versions can be found in Github repository under the *images/interactive/ks\_test* folder [17].



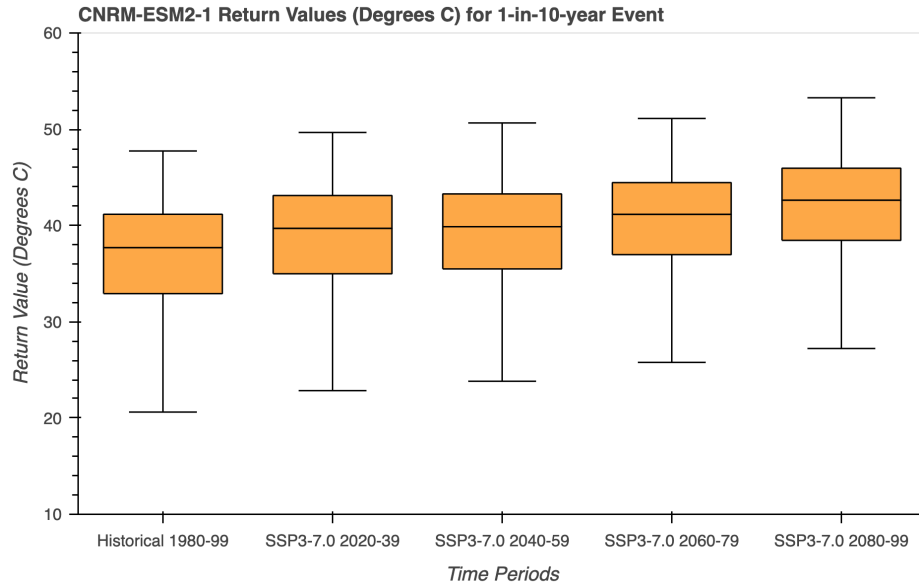
**Figure 3: CESM2 Return Values (Degrees C) for a 1-in-10-year Event.** Geospatial map of return value results for each 20-year temporal period. Interactive versions can be found in Github repository under the `images/interactive/return_value` folder [17].



**Figure 4: CNRM-ESM2-1 Return Values (Degrees C) for a 1-in-10-year Event.** Geospatial map of return value results for each 20-year temporal period. Interactive versions can be found in Github repository under the `images/interactive/return_value` folder [17].

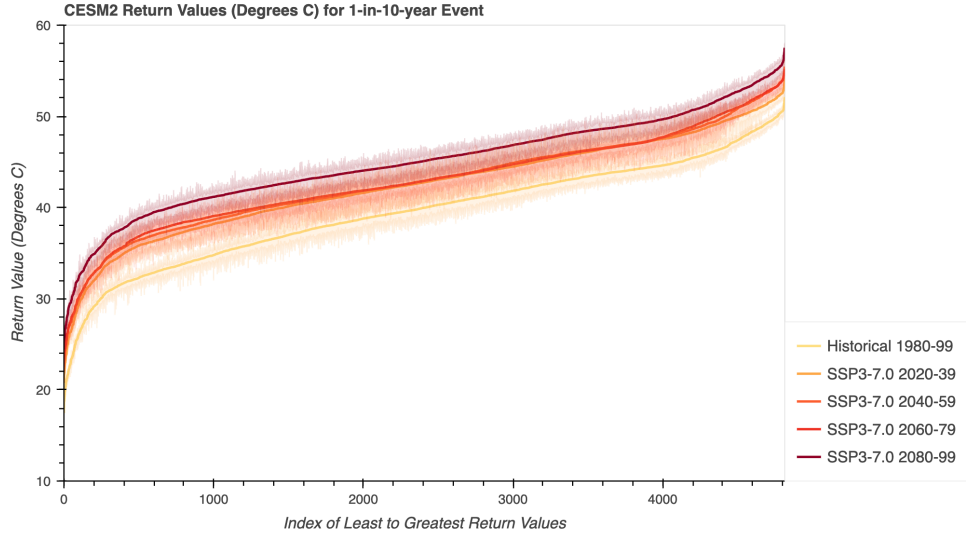


(a) CESM2

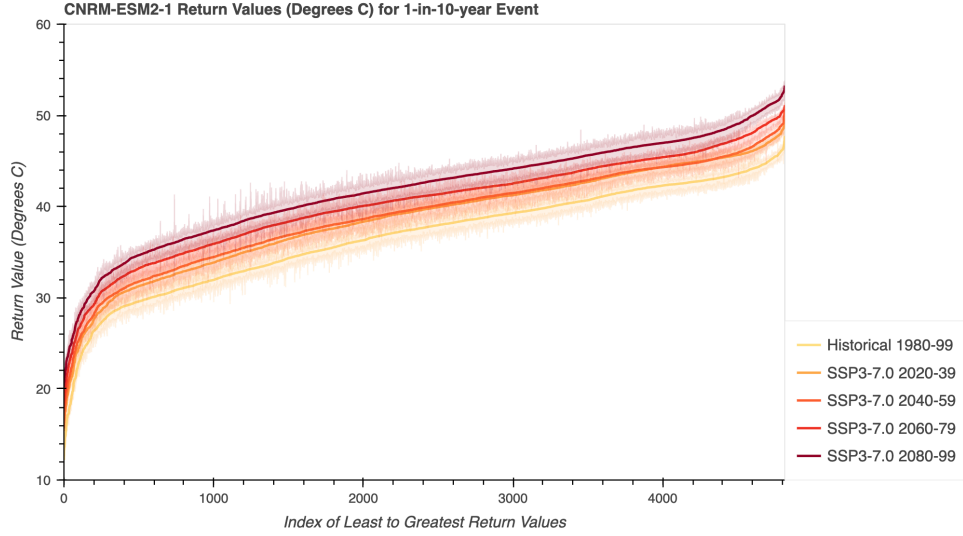


(b) CNRM-ESM2-1

Figure 5: **Box Plots of All Return Values.** Irrespective of geospatial information, all return value results for a 1-in-10-year event aggregated together by GCM.



(a) CESM2



(b) CNRM-ESM2-1

**Figure 6: Line Graph of Ordered Return Values.** Irrespective of geospatial information, all return value results for a 1-in-10-year event aggregated together by GCM and ordered from least to greatest value. The shaded area around each line is a confidence interval (2.5th percentile, 97.5th percentile) created through bootstrapping. Interactive versions can be found in Github repository under the *images/interactive/return\_value* folder [17].

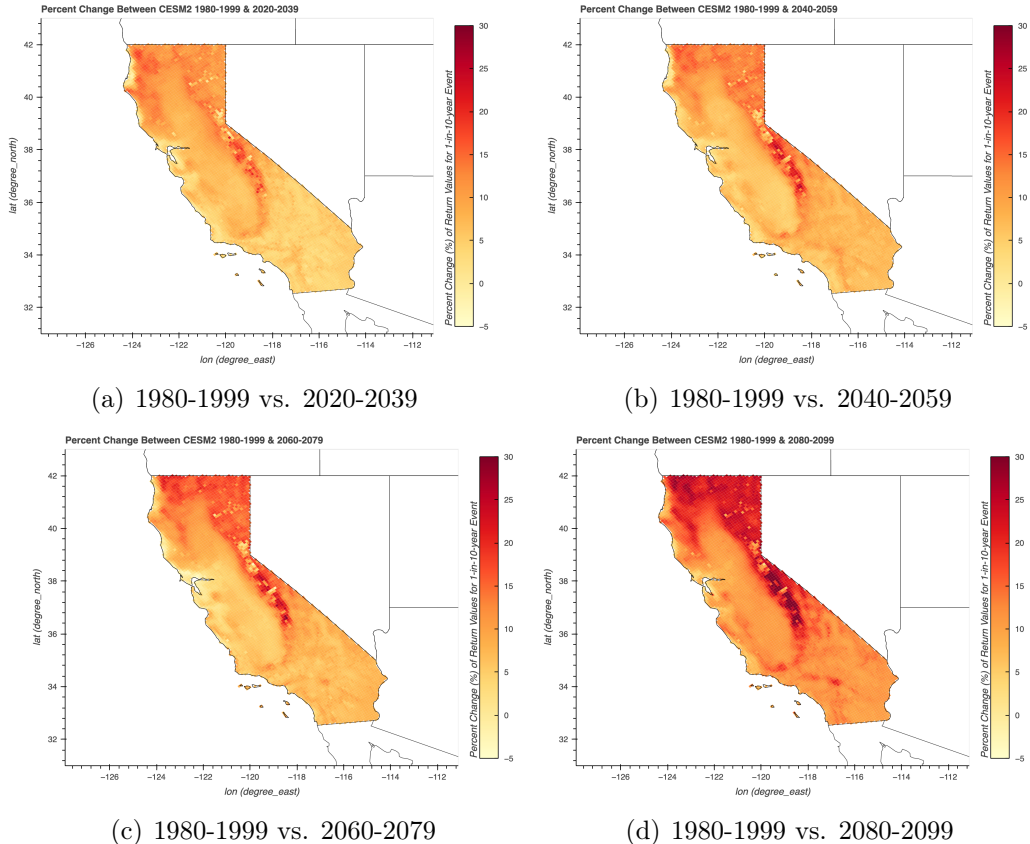


**Figure 7: CESM2 Percent Change (%) in Return Values Between Temporal Periods.** Geospatial map of percent change results of return value differences between baseline 20-year temporal period (1980-1999) and projected 20-year temporal periods. Interactive versions can be found in Github repository under the *images/interactive/percent\_change* folder [17].

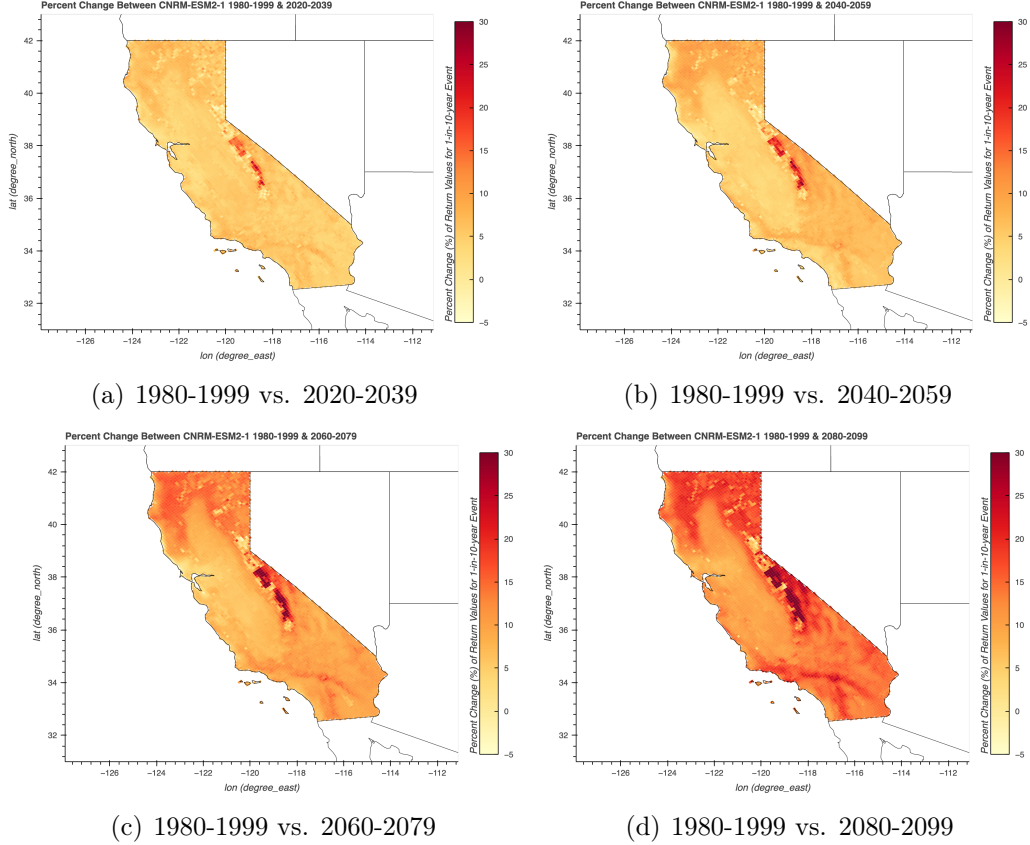
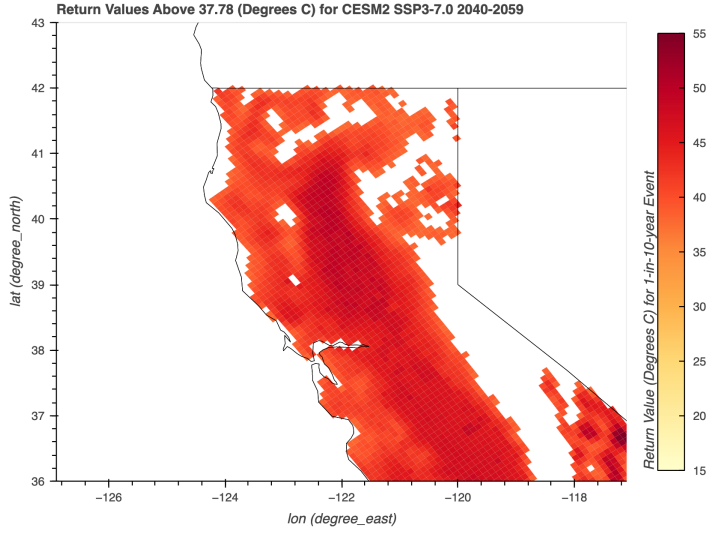
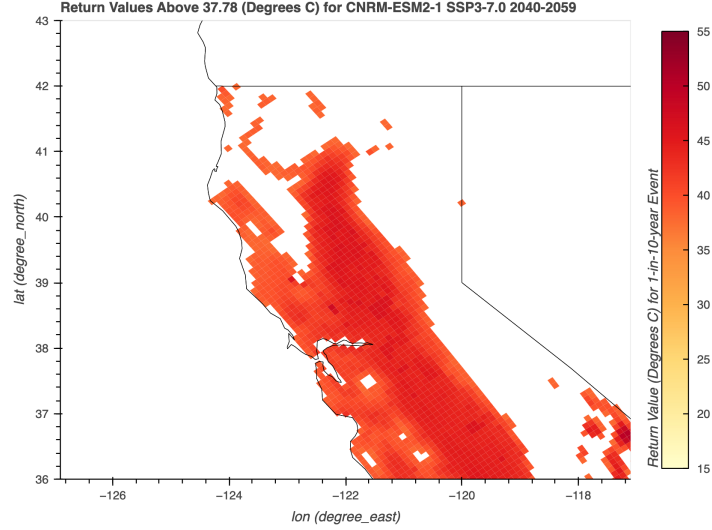


**Figure 8: CNRM-ESM2-1 Percent Change (%) in Return Values Between Temporal Periods.** Geospatial map of percent change results of return value differences between baseline 20-year temporal period (1980-1999) and projected 20-year temporal periods. Interactive versions can be found in Github repository under the *images/interactive/percent\_change* folder [17].



(a) CESM2



(b) CNRM-ESM2-1

**Figure 9: Capacity Loss Example of Return Values Above 37.78 (Degrees C) for a 1-in-10-year Event.** Geospatial map of return value results above 37.78 (Degrees C) for each 20-year temporal period. Interactive versions can be found in Github repository under the *images/interactive/return\_value* folder [17].

## 5 Conclusions

In this paper, I aimed to demonstrate how customizable analytics could be used for the characterization of extreme temperature events. Through EVA, I applied a methodological approach using L-moments and the GEV distribution for calculating the return values of 1-in-10-year temperature events. The results showcase not only how extreme temperature events are generally expected to intensify in magnitude up to 2100 but also how those trends vary by GCM, location, and temporal period.

I hoped to also illustrate how this flexible set of analytics could be applied to certain application use-cases, and produce relevant data products that allow for the extraction of decision-relevant insights on extreme weather exposure, climate impact, and vulnerability. These types of insights will be essential as climate change continues to alter the climatic impacts that will occur to our human and natural systems, and will ultimately allow for building more effective adaptation and resilience to them.

In terms of next steps, this analysis could be further refined by expanding to more particular application use-cases and data products, and including calculations on a range of return periods and return probabilities. To capture greater uncertainty and result variability, more GCMs and scenarios beyond SSP3-7.0 could also be utilized. Much of these additional features will take place as continued work through the Cal-Adapt Analytics Engine ([analytics.cal-adapt.org](http://analytics.cal-adapt.org)).

*Github Repository.* All code, datasets, and visualizations are publicly available in the open-source Github repository [17].

*Acknowledgements.* I would like to start off by thanking Andrew Jones and William Collins for all their support throughout this writing and research process. Their guidance, comments, and reviews were essential, and I'm grateful for their time. I would also like to thank the Cal-Adapt Analytics Engine team and Mark Risser for their support in building the tool and expanding my understanding of core concepts for this project. Lastly, I owe a great deal of gratitude to the broader UC Berkeley Energy and Resources Group (ERG) community and chosen family and friends for their care throughout this journey.

## References

- [1] C. Simolo, M. Brunetti, M. Maugeri, T. Nanni, and A. Speranza. Understanding climate change-induced variations in daily temperature distributions over italy. *Journal of Geophysical Research*, 115(D22), November 2010. doi: 10.1029/2010jd014088. URL <https://doi.org/10.1029/2010jd014088>.
- [2] Francis W. Zwiers and Viatcheslav V. Kharin. Changes in the extremes of the climate simulated by CCC GCM2 under CO<sub>2</sub>/subdoubling. *Journal of Climate*, 11(9):2200–2222, September 1998. doi: 10.1175/1520-0442(1998)011<2200:citeot>2.0.co;2. URL [https://doi.org/10.1175/1520-0442\(1998\)011<2200:citeot>2.0.co;2](https://doi.org/10.1175/1520-0442(1998)011<2200:citeot>2.0.co;2).
- [3] Melissa Dumas, Binita Kc, and Colin I. Cunliff. Extreme weather and climate vulnerabilities of the electric grid: A summary of environmental sensitivity quantification methods. Technical report, August 2019. URL <https://doi.org/10.2172/1558514>.
- [4] Ani Shabri, Zahrahtul Amani Zakaria, and Ummi Nadiah Ahmad. Flood frequency analysis of annual maximum stream flows using l-moments and tl-moments approach. *Applied Mathematical Sciences*, 5:243–253, 2011. URL <https://www.researchgate.net/publication/228430024>.
- [5] Francesco Laio, Giuliano Di Baldassarre, and Alberto Montanari. Model selection techniques for the frequency analysis of hydrological extremes. *Water Resources Research*, 45(7), July 2009. doi: 10.1029/2007wr006666. URL <https://doi.org/10.1029/2007wr006666>.
- [6] Christopher J. Paciorek, Dáithí A. Stone, and Michael F. Wehner. Quantifying statistical uncertainty in the attribution of human influence on severe weather. *Weather and Climate Extremes*, 20:69–80, June 2018. doi: 10.1016/j.wace.2018.01.002. URL <https://doi.org/10.1016/j.wace.2018.01.002>.
- [7] Hanbeen Kim, Sooyoung Kim, Hongjoon Shin, and Jun-Haeng Heo. Appropriate model selection methods for nonstationary generalized extreme value models. *Journal of Hydrology*, 547:

- 557–574, April 2017. doi: 10.1016/j.jhydrol.2017.02.005. URL <https://doi.org/10.1016/j.jhydrol.2017.02.005>.
- [8] Amir Aghakouchak, Elisa Ragno, Charlotte Love, and Hamed Moftakhari. Projected changes in California's precipitation intensity-duration-frequency curves, 8 2018. URL [https://www.energy.ca.gov/sites/default/files/2019-11/CCCA4-CEC-2018-00\\_ADA.pdf](https://www.energy.ca.gov/sites/default/files/2019-11/CCCA4-CEC-2018-00_ADA.pdf).
  - [9] Romany M Webb, Michael Panfil, and Sarah Ladin. Climate risk in the electricity sector: Legal obligations to advance climate resilience planning by electric utilities, 2020. URL <https://ssrn.com/abstract=3800497>.
  - [10] Joseph J. Barsugli, Galina Guentchev, Radley M. Horton, Andrew Wood, Linda O. Mearns, Xin-Zhong Liang, Julie A. Winkler, Keith Dixon, Katharine Hayhoe, Richard B. Rood, Lisa Goddard, Andrea Ray, Lawrence Buja, and Caspar Ammann. The practitioner's dilemma: How to assess the credibility of downscaled climate projections. *Eos, Transactions American Geophysical Union*, 94(46):424–425, November 2013. doi: 10.1002/2013eo460005. URL <https://doi.org/10.1002/2013eo460005>.
  - [11] Western Electricity Coordinating Council. Extreme natural event study report, 5 2022. URL <https://www.wecc.org/Administrative/Extreme%20Natural%20Event%20Study%20Report%202-22-2022%20Rev%201.0.docx>.
  - [12] Nathaniel B. Guttman. The use of l-moments in the determination of regional precipitation climates. *Journal of Climate*, 6(12):2309–2325, December 1993. doi: 10.1175/1520-0442(1993)006<2309:tuolmi>2.0.co;2. URL [https://doi.org/10.1175/1520-0442\(1993\)006<2309:tuolmi>2.0.co;2](https://doi.org/10.1175/1520-0442(1993)006<2309:tuolmi>2.0.co;2).
  - [13] N. Vivekanandan. Flood frequency analysis using method of moments and l-moments of probability distributions. *Cogent Engineering*, 2 (1):1018704, March 2015. doi: 10.1080/23311916.2015.1018704. URL <https://doi.org/10.1080/23311916.2015.1018704>.
  - [14] S. Saeid Eslamian and Hussein Feizi. Maximum monthly rainfall analysis using l-moments for an arid region in isfahan province, iran. *Journal*

- of Applied Meteorology and Climatology*, 46(4):494–503, April 2007. doi: 10.1175/jam2465.1. URL <https://doi.org/10.1175/jam2465.1>.
- [15] Neslihan Seckin, Tefaruk Haktanir, and Recep Yurtal. Flood frequency analysis of turkey using l-moments method. *Hydrological Processes*, 25(22):3499–3505, April 2011. doi: 10.1002/hyp.8077. URL <https://doi.org/10.1002/hyp.8077>.
  - [16] Songzhe Zhu, Yi Zhang, D Le, and A A Chowdhury. Understanding stability problems in actual system &#x2014; case studies. In *IEEE PES General Meeting*. IEEE, July 2010. doi: 10.1109/pes.2010.5590041. URL <https://doi.org/10.1109/pes.2010.5590041>.
  - [17] Nabig Chaudhry. Masters project, 2022. URL [https://github.com/nabigac/masters\\_project](https://github.com/nabigac/masters_project).
  - [18] Alex Hall. CMIP6 Downscaling Using WRF, 2022. <https://dept.atmos.ucla.edu/alexhall/downscaling-cmip6>, accessed 2022-04-09.
  - [19] Claudia Tebaldi, Kevin Debeire, Veronika Eyring, Erich Fischer, John Fyfe, Pierre Friedlingstein, Reto Knutti, Jason Lowe, Brian O'Neill, Benjamin Sanderson, Detlef van Vuuren, Keywan Riahi, Malte Meinshausen, Zebedee Nicholls, George Hurtt, Elmar Kriegler, Jean-Francois Lamarque, Gerald Meehl, Richard Moss, Susanne E. Bauer, Olivier Boucher, Victor Brovkin, Jean-Christophe Golaz, Silvio Gualdi, Huan Guo, Jasmin G. John, Slava Kharin, Tsuyoshi Koshiro, Libin Ma, Dirk Olivié, Swapna Panickal, Fangli Qiao, Nan Rosenbloom, Martin Schupfner, Roland Seferian, Zhenya Song, Christian Steger, Alistair Sellar, Neil Swart, Kaoru Tachiiri, Hiroaki Tatebe, Aurore Voltaire, Evgeny Volodin, Klaus Wyser, Xiaoge Xin, Rong Xinyao, Shuting Yang, Yongqiang Yu, and Tilo Ziehn. Climate model projections from the scenario model intercomparison project (ScenarioMIP) of CMIP6. September 2020. doi: 10.5194/esd-2020-68. URL <https://doi.org/10.5194/esd-2020-68>.
  - [20] J. R. M. Hosking. L-moments: Analysis and estimation of distributions using linear combinations of order statistics. *Journal of the Royal Statistical Society: Series B (Methodological)*, 52(1):105–124, September 1990. doi: 10.1111/j.2517-6161.1990.tb01775.x. URL <https://doi.org/10.1111/j.2517-6161.1990.tb01775.x>.

- [21] Florenz A P Hollebrandse, Sam Gillespie, William Asquith, and J. R. M. Hosking. lmoments3 library documentation release 1.0.2, 2015.